Lawrence Berkeley National Laboratory

Title
THE EXTERNAL MUON IDENTIFIER FOR THE FERMILAB 15-FT BUBBLE CHAMBER

Permalink
https://escholarship.org/uc/item/2sn951cb

Author
Cence, R.J.

Publication Date
1976-06-01

0 0 0 0 4 5 0 1 9 8 6

RECEIVED
LAWRENCE
BERKELEY LABORATORY

THE EXTERNAL MUON IDENTIFIER FOR THE
FERMILAB 15-FT BUBBLE CHAMBER

R. J. Cence, F. A. Harris, S. I. Parker, M. W. Peters,
V. Z. Peterson, V. J. Stenger, G. Lynch, J. Marriner,
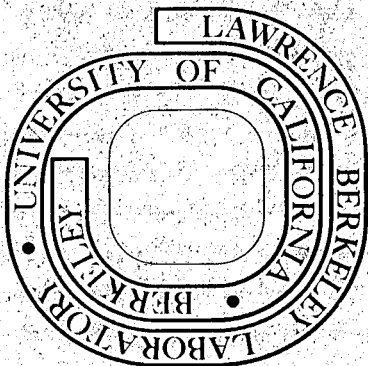F. Solmitz, and M. L. Stevenson

June 1976

DISCLAIMER

THE EXTERNAL MUON IDENTIFIER FOR THE FERMILAB 15-FT BUBBLE CHAMBER[*]

R. J. Cence, F. A. Harris, S. I. Parker, M. W. Peters,
V. Z. Peterson, V. J. Stenger

Department of Physics
University of Hawaii
Honolulu, Hawaii 96822

and

G. Lynch, J. Marriner, F. Solmitz, M. L. Stevenson

Lawrence Berkeley Laboratory
University of California
Berkeley, California 94720

ABSTRACT

An external muon identifier to aid in the identification of
muons produced in neutrino interactions in the Fermilab 15-ft bubble
chamber has been constructed. Details of design and analysis
procedures are discussed. The spatial resolution and efficiency
have been calibrated using muons regenerated by neutrino interactions
in material upstream of the bubble chamber. A formalism to describe
the statistical significance of muon matches in the identifier is
developed and tested using tracks from actual neutrino interactions.

I. Introduction

In the study of neutrino interactions using intense beams of muon neutrinos such as are produced at Fermi National Accelerator Laboratory, muon identification is of prime importance. This importance has been underscored by the discoveries of neutral current[1] and di-lepton[2] events. In 1970, an External Muon Identifier (EMI) was proposed[3] to aid in identifying muons emerging from interactions within the Fermilab 15-ft Bubble Chamber. Tests of the proposed method to separate hadrons and muons were conducted using a 3 GeV/c meson beam at the Bevatron in 1971[4]. A somewhat scaled down version of the proposal was approved and became operational during the summer of 1974, in time for the first bubble chamber operation with neutrinos incident on hydrogen. The EMI has subsequently been used by several groups in experiments to study neutrino and antineutrino interactions on both hydrogen and mixtures of neon-hydrogen, and with both 300 GeV and 400 GeV protons incident on the neutrino target.

Muon identification for neutrino interactions in the 15-ft bubble chamber is complicated by the fact that not only is the muon source a large volume, but, further, the muons emerge with a wide range of angles and momenta. The problem is solved with a large area, single plane detector mounted on the vacuum tank of the bubble chamber to measure the positions of all tracks emerging from a relatively thin absorber of 3-5 absorption lengths located inside the vacuum tank. Some of these tracks are associated with neutrino interactions inside the bubble chamber, but most arise from interactions in the absorber or other material surrounding the sensitive volume of the

bubble chamber. Interactions of interest within the bubble chamber are located by scanning the film; then each track is measured to determine its position and momentum. Using the known magnetic field, it is then possible to calculate the position of each track at the detector plane and to predict a region in which the probability of finding the particle will be high if, indeed, it is a muon. Hadrons usually undergo strong interactions in the absorber and will frequently be completely absorbed, scatter out of the acceptance region, or produce hadron cascades. Thus, they may reveal their identity by producing no particles in the acceptance region or many particles in the region of the extrapolated track. (The latter case has not yet proved to be very useful.) Some muons are lost because of detector inefficiencies, and others (a known fraction) are lost because they are on the tails of the multiple Coulomb scattering distribution. On the other hand, some hadrons are mistaken as muons because: (a) they have, within the acceptance region, either a (background) track from an unrelated interaction or a secondary from an interaction of the hadron in the absorber, or (b) they fail to interact in the absorber.

II. Experimental Apparatus

The EMI apparatus is shown schematically in Fig. 1. The detector plane consists of an array of 24 multiwire proportional chambers (MWPC), each with a sensitive area of one square meter. They are arranged three high by eight wide and cover approximately 135° azimuthally and 45° vertically. The chambers are overlapped to eliminate the possibility that particles will pass between chambers. Proportional chambers were chosen for this application because they provide the

required resolution to separate scattered hadrons from muons, require no trigger, are continuously sensitive, and operate well in the large non-uniform fringe field of the bubble chamber superconducting magnet.

The geometric muon acceptance for the conditions corresponding to the first bubble chamber photographs (neutrinos on hydrogen) has been calculated using a Monte Carlo program[5]. For this period, 300 GeV protons were incident on an aluminum target, and the secondary mesons were focused by a single magnetic horn. Muons from Monte Carlo generated charged current neutrino interactions inside a 20 m^3 fiducial volume were extrapolated through the magnetic field (21 kG at the center of the bubble chamber), and the fraction striking the EMI detector was determined to be 87%. For those events with a total visible momentum greater than 10 GeV/c, it was 89%.

The hadron absorber is composed of the material in the bubble chamber superconducting magnet coils and support structure with additional zinc added between and behind the coils. Zinc was chosen because it is an inexpensive, non-magnetic, relatively low Z material with reasonable density. The conductor of the magnet coils is wound into flat rings, 3.8 cm thick separated by 0.3 cm gaps. In the analysis of the data, this fine structure is ignored, however, and a uniform, homogeneous absorber with the same average density is assumed. The magnet coils, which are approximately 2/3 copper and 1/3 stainless steel, are slightly over two absorption lengths thick. The absorption lengths used are indicated in Table 1. Three absorption lengths of zinc blocks (7 metric tons) have been stacked in three port holes

in the magnet support structure, and another 6 metric tons of zinc has been added between the coils but inside the magnet cryostat. After the early 1974 hydrogen exposures, an additional 30 metric tons of zinc was added just behind the magnet cryostat. With the present absorber, a typical muon passes through 3 to 5 absorption lengths of material.

The MWPC's[6] are constructed with a single 20 μm diameter wire plane and two photo-etched cathode planes made of gold plated copper bonded to mylar. The copper strips on one cathode plane are perpendicular to the wire plane and at a 45° angle on the other. The wire plane and two cathode planes provide measurements of time and three (one redundant) spatial coordinates when used with electromagnetic delay line readout. The cathode planes are supported by honeycomb panels and spaced 8 mm from the wires by a picture frame of G-10 fiberglass. The proportional chambers, delay lines, and associated electronics are mounted in aluminum boxes which also provide electromagnetic shielding. The overall size of the package is 127 cm × 127 cm × 7 cm.

The use of electromagnetic delay lines with typical delay times of 10 μsec/meter allows coordinate readout at a large cost savings over conventional amplifier per wire systems. There are four 1-meter long delay lines per module: one each for the x and y axes, and one for each half of the diagonal or u axis. They are physically arranged as shown in Fig. 2. The x and y delay lines have an amplifier at each end, but the u delay lines, for reasons of economy, have only one amplifier each. A seventh amplifier, which is attached between the

central conductor of the y delay line and ground, produces a prompt
pulse nearly coincident with the time (t) of the avalanche at the anode
wire of the MWPC. The pulses from the other amplifiers occur at
various delayed times determined by the spatial coordinates x and y
and the velocities of a propagation down the delay lines. Passage
of a particle through the chamber injects a pulse on the x delay
line, for example, at a distance x from one end. The pulse arrives
at the opposite ends (labeled XA and XB) of the delay line at times
given by

$$t_{XA} - t_{XA_0} = x/v_x + t$$

$$\text{(1)}$$

$$t_{XB} - t_{XB_0} = (\ell - x)/v_x + t$$

where ℓ is equal to 102.6 cm, the width and height of the active area
of the MWPC, v_x is the delay line velocity, and t_{XA_0} and t_{XB_0} are
constant time delays. Similarly the Y delay line reads out times

$$t_{YA} - t_{YA_0} = y/v_y + t$$

$$\text{(2)}$$

$$t_{YB} - t_{YB_0} = (\ell - y)/v_y + t$$

and the diagonal U delay line

$$t_{UA} - t_{UA_0} = (x - y)/v_{UA} + t \quad \text{if} \quad x > y$$

$$\text{(3)}$$

$$t_{UB} - t_{UB_0} = (y - x)/v_{UB} + t \quad \text{if} \quad y > x$$

The prompt amplifier measures t directly

$$t_P - t_{P_0} = t$$

$$\text{(4)}$$

The output of the amplifiers is a 200-1000 mV (typical) positive pulse which travels along 160 m of coaxial cable to the EMI control room where it is applied to a discriminator. The discriminator consists of two parts: the first part is an amplifier with a variable gain which differentiates the input pulse, and the second is a zero crossing circuit. The zero crossing circuit is activated by a minimum voltage and triggers when the differentiated wave crosses zero. In terms of the input pulse, the discriminator is activated by a minimum rate of change of voltage $\left(\frac{dV}{dt}\right)$, and triggers at the peak. The overall threshold of the discriminator is adjusted by setting the gain of the input amplifier. The use of a zero-crossing type discriminator to find the center of the pulse is essential since the pulses are several hundred nanoseconds wide, while the time resolution must be 30 nsec or less. The output of the discriminators is digitized by a CAMAC system which employs a 28 MHz clock. Clock pulses are scaled, and the contents of the scaler are recorded in a scratch pad memory upon the arrival of a discriminator pulse. Up to 16 pulses may be recorded for each amplifier. A more complete description of the electronics has been given elsewhere[7]. Between beam spills, the memories are read out by a PDP-11 computer and then written onto magnetic tape.

Since the EMI detector consists of a single plane, detecting inefficient MWPC chambers is difficult. Fortunately, the redundancy within each of the proportional chambers may be used for this purpose. The online computer operating system uses cosmic rays between accelerator pulses to determine that each proportional chamber records cosmic rays at approximately the proper rate, and that a preset fraction

(usually 65%) of uncomplicated events has a single encoding from each
of six amplifiers. Cosmic rays are also used to adjust the dis-
criminator thresholds, so that each amplifier makes one encoding
for each cosmic ray as often as possible while encoding extra unwanted
pulses as seldom as possible. An elaborate system of hardward checks
performed under computer control insures that the electronics is
operating properly.

III.   Analysis Procedures

In order to use the 15-ft Bubble Chamber/EMI hybrid system, it
is necessary to match bubble chamber tracks to particle hits in the
EMI chambers. Two computer programs in addition to the usual bubble
chamber geometry program are required. The first program constructs
all possible (x,y,t) fits from the raw time digitizations for each
EMI chamber. The second program extrapolates the bubble chamber
tracks to the EMI and compares the observed fitted x and y positions
to the extrapolated positions.

Since the time between particles is comparable to the total delay
time of a delay line, it is not uncommon for the time order of the
arrival of pulses from a given amplifier to differ from the time
ordering of the passage of the particles which initiated them. The
MWPC coordinate fitting program then must carry out two functions:
the association of related encodings and the calculation from these
of the particle coordinates. In addition, several circumstances may
interfere with the arrival of pulses at the digitizer modules and
with their accurate encoding. First, signals traveling the full

length of a delay line and coming from particles with low primary

ionization may be lost because of attenuation. A pulse is attenuated

by about 0.5 when traveling the length of the delay line. Second, a

pulse may be lost if it follows another too closely on a delay line.

The pulse-to-pulse resolution, i.e., the minimum separation for which

two encodings are reliably produced at both ends of the delay line,

is 0.5 μsec (65 mm on the y delay line). This distance is 6.5% of the

total length of the delay line, so coincidences leading to loss of

encodings are not a negligible effect. This separation is needed for

a small pulse following a large pulse to count. At the end of the

delay line where the small pulse leads, somewhat less than half this

separation is necessary.

In addition, coincident pulses on either delay line or the prompt

channel may saturate the amplifier, producing a flat-topped pulse.

Such pulses lead to an encoding representing the beginning of the flat

top rather than the center of the pulse. This "pulling" of the encoding

is only expected to be important when several simultaneous particles

hit the same MWPC (as in a shower).

Finally, small but significant couplings between amplifiers can

give unwanted extra pulses. Additional encodings may also be present

as a result of electromagnetic interference or small high voltage

discharges within the chamber. The additional encodings may appear

in a wide variety of ways, varying both in frequency and in the

number of channels which are active.

Thus, the reconstruction must allow for an arbitrary overlapping

of events and for inefficiencies and noise encodings in arbitrary

combinations. If all encodings are present, there are six pieces of

data available $(t_P, t_{XA}, t_{XB}, t_{YA}, t_{YB}, t_U)$, where t_U may be either

t_{UA} or t_{UB}, depending upon whether the hit was above or below the

chamber diagonal. There are three quantities to be determined for

each hit (t,x,y) so there are three excess quantities beyond those

needed for a direct solution. A 3-constraint (3C) least squares fit

may therefore be performed using Eqs. (1)-(3). If 1, 2, or 3 encodings

are missing, the fit becomes 2C, 1C, or 0C respectively. A good

solution must have one or more constraints, a sufficiently small chi-

squared, and must use some encoding which has not been used by a

solution of a higher constraint class. This latter requirement

eliminates spurious fits such as $(t_P, t'_{XA}, t'_{XB}, t_{YA}, t_{YB})$ where

$(t_P, t_{XA}, t_{YA}, t_{YB}, t_U)$ and $(t_P, t'_{XA}, t''_{XB}, t'_{YA}, t'_{YB}, t'_U)$ are both

good 3C fits. Even with this restriction, spurious or ghost solutions

may be found. Two different computer programs[8] have been written to

perform the reduction of the MWPC data; they produce nearly identical

results.

Before the fitting program can be used, the eleven constants

appearing in Eqs. (1)-(3) must be determined for each MWPC. Four

of these are delay line velocities, and the other seven are constant

time delays for each amplifier channel. Seven constants may be

determined from a χ^2 minimization technique, using events each with a

$t_P, t_{XA}, t_{XB}, t_{YA}, t_{YB}$, and t_{UA} or t_{UB} encoding. However, the origin

of the readout system relative to the chamber remains undetermined

as does the origin in time. Also indeterminate is the overall scale

of the readout system, i.e., only the ratios of the velocities can

be determined by the χ^2 minimization. The problem is greatly alleviated by the use of fiducial pulses which are applied to the delay lines in places referenced to the MWPC. In principal, the fiducial pulses allow a complete calibration of all MWPC delay line constants. However, the fiducial pulses give slightly biased estimates of delay line constants since their pulse shapes differ somewhat from those of actual chamber pulses. In practice, the fiducials give a first estimate of MWPC delay line constants; the χ^2 minimization is then used for those constants which it determines[9]. The quantities undetermined by the χ^2 minimization are accurately calibrated, as will be described later, by using tracks seen in the bubble chamber.

The second computer program extrapolates bubble chamber tracks through the absorber to the proportional chambers by integrating the equations of motion of a particle subject to a magnetic field and energy loss in a medium. The extrapolated position is an average expected position whose deviations are due to measurement errors in the bubble chamber and multiple Coulomb scattering in the absorber. The proper calculation of these errors is necessary in order to describe the statistical significance of the matches between extrapolated positions and actual positions as reconstructed by the MWPC fitting program. The Coulomb scattering deviations are calculated by a standard method[10], while the momentum and angle errors from the bubble chamber film measurements are propagated to the EMI in a small turning angle approximation. The proportional chamber and bubble chamber spatial resolutions are combined and taken to be 0.33 cm, a number determined from the confidence level distribution of high energy muons.

All the above added in quadrature yield the expected rms deviation σ

of the appropriate MWPC fit about the extrapolated value if the track

is a muon. The rms scattering of an average track in the absorber

is given roughly by 10/P cm, where P is the momentum in GeV/c. At

very high momentum (above 20 GeV), the resolution of the MWPC and

bubble chamber is usually the dominant contribution to σ, while at

lower energies Coulomb scattering usually dominates.

IV. EMI Calibration

The proportional chamber positions were initially determined by

measurements relative to the vacuum tank of the bubble chamber. A

precise determination of their positions, but relative to the bubble

chamber fiducials, was made with a sample of high energy muons

consisting of single tracks in the bubble chamber with momenta greater

than 10 GeV/c and which make an angle of less than 2.5° with respect

to the neutrino beam direction in both dip and azimuth. The hadron

contamination of this sample was estimated to be 0.8 ± 0.3% by

observing the ratio of interacting to non-interacting tracks and

correcting for the interaction probability. By comparing the data

from the proportional chamber with the position extrapolated from the

bubble chamber, the best values of s, x_0, and y_0 in the equations

$$x' = sx + x_0$$

$$y' = sy + y_0$$

(5)

are found. In the above, x and y are the MWPC coordinates obtained

with the calibration described in section III, and x' and y' are the

corrected MWPC coordinates after the final calibration with muons.
Figure 3 shows the results of a calibration of one chamber. Not all
chambers can be calibrated in this manner because only proportional
chambers directly behind the sensitive volume of the bubble chamber
intercept fast muons. However, it is not necessary to have precise
locations for the peripheral chambers, since muons intercepted by
them are of low momenta and have rather large multiple Coulomb scattering
regions.

The same sample of muons has been used to study the error
distribution of track matches in the proportional chambers. The
behavior of $\Delta x/\sigma_x$ where Δx is the difference between the extrapolated
position and the observed position in the MWPC and σ_x is the expected
rms deviation was found to be non-Gaussian. The distribution is, however,
well fitted by the sum of two Gaussian distributions. The dominant
features of the distribution are well fitted by a Gaussian of width
σ_x, but some additional component due to a Gaussian of width
$\sigma'^2_x = \sigma^2_x + (1.7 \text{ cm})^2$ is necessary to describe events with large Δx.
The second Gaussian, which amounts to about 10% of the events, is
understood to be due to the imperfect two pulse resolution: additional
undesired pulses may be due to δ rays, a chance coincidence of unrelated
events, or any of the sources discussed in section III. Using a
pulse which is near to, but not identical with, the true position thus
produces a considerably poorer MWPC resolution. From the data, it
is found that the confidence level C is uniformly distributed between
0 and 1, if

$$C = (1 - \delta) \exp \frac{-1}{2}\left(\frac{\Delta x^2}{\sigma_x^2} + \frac{\Delta y^2}{\sigma_y^2}\right) + \delta \exp -\frac{1}{2}\left(\frac{\Delta x^2}{\sigma_x'^2} + \frac{\Delta y^2}{\sigma_y'^2}\right) \qquad (6)$$

with $\delta = 0.1$, Δy and σ_y' are defined similarly to Δx and σ_x'.

The muons can also be used to determine the MWPC efficiency since the hadron contamination is small. In a sample of 4012 tracks, 209 had EMI matches with a confidence level between 0 and 0.01. After correcting for the 0.8% hadron contamination and the 1% of events expected to populate this range of confidence level, the residual inefficiency is 4%. The inefficiency is caused largely by the same processes as cause the broadening of the MWPC resolution, except that instead of forming nearby solutions, solutions are lost completely because of missing encodings. There is also a contribution from events whose primary ionization is low, and the pulse heights from the delay lines are insufficient to trigger the required 4 discriminator channels for a 1C fit.

V. Muon and Hadron Confidence Levels

It is advantageous to define two quantities, p_μ and p_h, where p_μ is the probability that a muon will give a worse fit than this track, and p_h is the probability that a hadron will give a better fit than this track. These quantities evaluate the probabilities of rejecting a true hypothesis (missing a muon) or accepting a false hypothesis (calling a hadron a muon). A well identified muon then is a track with a large p_μ and a small p_h. The calculated probabilities must include the effects of multiple scattering of muons and non-interacting hadrons, EMI and bubble chamber track location errors, efficiency of

the EMI chambers, spatial coincidences with unrelated EMI hits (random background), and the spatial distribution of interacting hadrons which penetrate the absorber (punch-through).

The spatial distribution of muons and non-interacting hadrons about the extrapolated track is described by the confidence level (Eq. (6)). Defining χ^2 and β by

$$\chi^2 = \left(\frac{\Delta x}{\sigma_x}\right)^2 + \left(\frac{\Delta y}{\sigma_y}\right)^2$$

$$\tan\beta = \frac{\Delta y \sigma_x}{\Delta x \sigma_y}$$

the equation may be rewritten as

$$C = (1 - \delta) \exp -\left(\frac{\chi^2}{2}\right) + \delta \exp\left[\frac{-\chi^2}{2} (\xi^+ + \xi^- \cos 2\beta)\right]$$

where

$$2\xi^+ = \left(\frac{\sigma_x}{\sigma'_x}\right)^2 + \left(\frac{\sigma_y}{\sigma'_y}\right)^2$$

and

$$2\xi^- = \left(\frac{\sigma_x}{\sigma'_x}\right)^2 - \left(\frac{\sigma_y}{\sigma'_y}\right)^2 \quad .$$

The confidence level depends on two random variables χ^2 and β, but nearly all of the dependence is on χ^2 because δ is small and ξ^- tends to be much smaller than ξ^+.

The probability that a hadron interacts before reaching the EMI without producing a secondary which passes near the extrapolated position is given by

$$\text{Prob} = 1 - \exp(-\Sigma \ell_i / \lambda_i')$$

where ℓ_i = path length, and λ_i' = absorption length, and the sum $\Sigma \ell_i / \lambda_i'$ is accumulated for all of the various materials encountered as the track is extrapolated out to the EMI chambers.

Background hits in the EMI may accidentally coincide with the extrapolated position of a hadron that has interacted, thus, making it look like a non-interacting muon. This effect is small for tracks that extrapolate to the EMI with small errors, but may be important for low momentum or poorly measured tracks where the calculated error, and, thus, the allowed region for a good hit is large. Sometimes this effect will also cause the nearest hit to an extrapolated muon not to be due to the muon itself, and may even "save" a muon for which the EMI was inefficient. The observed value of χ^2 defines an elliptical region of the EMI within which any hit would be better than the observed hit. The probability of getting no background hits within this ellipse is taken as the Poisson probability

$$\text{Prob} = e^{-\rho(\text{Area})} = \exp(-\rho \pi \sigma_x \sigma_y \chi^2)$$

where ρ is the area density of hits. This form for the background assumes that it is random and that the EMI array is infinite. In practice the expression for background should be adequate for areas $<1 \text{ m}^2$.

Early evidence indicates that punch through does not seem to be very sharply peaked about the extrapolated track position. Therefore, we assume that it is uniformly distributed and is included in the general background of random EMI hits.

Combining all the effects, p_μ and p_h may be written

$$p_\mu = [1 - \varepsilon] \cdot [C] \cdot \left[\exp\left(-\rho\pi\sigma_x\sigma_y\chi^2\right)\right] + [\varepsilon] \cdot \left[\left(\exp -\rho\pi\sigma_x\sigma_y\chi^2\right)\right] \tag{7}$$

$$\begin{bmatrix} \text{EMI} \\ \text{Works} \end{bmatrix} \text{ and } \begin{bmatrix} \mu \\ \text{Scatters} \\ \text{Outside} \end{bmatrix} \text{ and } \begin{bmatrix} \text{No Background} \\ \text{Inside} \end{bmatrix} \text{ or } \begin{bmatrix} \text{EMI} \\ \text{Fails} \end{bmatrix} \text{ and } \begin{bmatrix} \text{No Background} \\ \text{Inside} \end{bmatrix}$$

$$1 - p_h = [1 - e^{-\ell/\lambda}] \cdot \left[\exp\left(-\rho\pi\sigma_x\sigma_y\chi^2\right)\right] + [e^{-\ell/\lambda}] \cdot [p_\mu] \tag{8}$$

$$\begin{bmatrix} \text{Hadron} \\ \text{Interacts} \end{bmatrix} \text{ and } \begin{bmatrix} \text{No Background} \\ \text{Inside} \end{bmatrix} \text{ or } \begin{bmatrix} \text{Hadron} \\ \text{does not} \\ \text{Interact} \end{bmatrix} \text{ and } \begin{bmatrix} \text{Hadron} \\ \text{Behaves Like} \\ \text{Muon} \end{bmatrix}$$

where ε is the EMI inefficiency. If the model is correct and if the proper values are used for ε, ℓ/λ, ρ, σ_x and σ_y, then by definition muons will uniformly populate p_μ and hadrons will uniformly populate p_h. The distribution of hadrons in terms of p_μ and of muons in terms of p_h is not given <u>a priori</u>, but depends on the distribution of tracks in terms of the parameters ℓ/λ, σ_x, and σ_y. Generally, however, the EMI separates muons from hadrons by the fact that muons tend to concentrate at low p_h, while hadrons concentrate at low p_μ (namely, hadrons are not likely to hit near the extrapolated track). It should be emphasized that for a particular track p_μ and p_h are correlated: if ξ^- is zero, the correlation is 100%. It should also be noted that tracks which go through essentially no absorber may still give values of p_μ and p_h which seem to imply that they are well identified muons.

VI. Comparison with Data

Neutrino events from the early hydrogen runs have been used to determine the parameters ρ and λ which appear in the expressions for p_μ and p_h and to evaluate the validity of the assumptions concerning background and penetration of hadrons through the absorber. A sample of hadrons with little muon contamination was obtained from a fairly pure sample of charged current neutrino events. The sample consists of events where the negative track with the highest transverse momentum[11] relative to the neutrino beam direction matches the predicted position (with $p_\mu > 0.15$). The remaining tracks in the event have a muon contamination of about 1%. Hadron tracks are separated into two categories. Those with EMI matches in time coincidence with the muon are used to determine λ, while those with matches out of time are used to determine ρ.

There are two components to the set of hadron tracks which have matches in time coincidence with the muon. The MWPC fits of the first component closely match the extrapolated position, while the second is distributed diffusely about the extrapolated position. This latter component is due to punch-through of the track in question, other tracks in the event, or possibly δ rays associated with the muon and is sufficiently diffuse to be treated as part of the background. Background, then, has both in time and out of time components.

At first it might seem sufficient to determine ρ by counting the average number of hits per chamber. However, it is important to use tracks from actual neutrino events in selecting chambers in the

determination of ρ because other nearby tracks in the neutrino events also contribute to the background. The contribution of these other tracks may not necessarily be in the form of MWPC fits which are in time with the event since these tracks may by chance make encodings which the MWPC reconstruction program uses to generate false solutions.

In the data sample considered, the distribution of the number of fits in a proportional chamber follows approximately a Poisson distribution for low numbers of fits but has a long tail which is presumably due to showers. To approximate the distribution, parameter ρ appearing in Eqs. (7) and (8) is set equal to the number of fits in the chamber if there is a "shower" (more than 6 fits) but is taken to be some average value when the chamber has fewer than 6 fits.

The average value of ρ when there are fewer than 6 fits in the chamber is determined from the neutrino events. The fraction $f(A)$ of tracks which match a background fit with the chi-square of the match equal to or smaller than χ^2 is $f(A) = 1 - e^{-\rho A}$, where $A = \pi\sigma_x\sigma_y\chi^2$. Solving for ρ:

$$\rho(A) = \frac{-\ln[1 - f(A)]}{A} \qquad (9)$$

Although ρ was assumed to be a constant in the derivation of Eqs. (7) and (8) in section V, the data which determine $f(A)$ will require a dependence on A. Displaying $\rho(A)$ as a function of A allows a determination of the validity of the assumption ρ = constant.

The function $f(A)$ is found by selecting tracks from the sample of hadrons where the EMI proportional chamber fit which is closest to the extrapolated position of the track is not in time coincidence with the

muon in the event. The criteria for time coincident fits was taken to be ±360 ns a value much larger than the proportional chamber time resolution (σ = 30 ns) but small compared to neutrino beam spill time (20 μsec). The distribution in the area A of these out of time fits determines f(A) which in turn yields ρ(A) through Eq. (9). Except for a sharp peak near the extrapolated position, tracks whose closest MWPC fit is in time have roughly the same diffuse spatial distribution as those with the closest fit out of time. Thus the elimination of tracks with the closest fit out of time does not substantially alter the spatial distribution f(A), and therefore does not change the value of ρ(A). The ρ(A) calculated, then, includes the effects of both in time and out of time background.

Figure 4 shows ρ(A) as determined from the ν data. The decrease of ρ(A) as the area increases is understood to be due primarily to tha fact that the EMI array of chambers is not infinite. In fact, in searching for the closest fit, between 1 and 4 chambers will be examined depending on how close the extrapolated track is to the edge of the chambers. The finite size of the EMI not only places a limit on the maximum value A can take, but creates the decreasing trend in ρ as the area A expands to the point where it is not entirely covered by the EMI proportional chambers. The value chosen for ρ is not unique because of the slight dependence on A. The value ρ(o) = 2.5/m^2 has been used for the conditions of the early hydrogen exposures. The variation of ρ from chamber to chamber is small and has been neglected.

The time coincident matches which are sharply peaked about the extrapolated position are due to non-interacting tracks and the

forward component of the punch-through. An overall correction factor η is defined so that $\lambda'_i = \eta\lambda_i$, where the λ'_i are the correct absorption lengths, and the λ_i are the absorption lengths assumed (see Table I). The parameter η is determined by requiring the expected number calculated from the absorption lengths λ'_i to agree with the number of hadrons matching (confidence level >0.15) and in time coincidence with the muon. Figure 5 shows the behavior of η as a function of momentum. Although each data point is within errors of $\eta = 1$, there is a strong suggestion that the length increases with momentum, as suggested by a hadron shower Monte Carlo generation program[12]. In calculating η, the contamination of the sample due to muons has been neglected. The lowest momentum bin is higher because much of the diffuse component is included when the Coulomb scattering region becomes large.

As a final check, the distribution in p_μ and p_h of a statistically pure sample of hadrons and muons will be given. Figure 6 shows the p_μ and p_h distribution of the high energy muons that were used for calibration and efficiency checks. The events lying along the straight line with p_μ and p_h both large are due to tracks which pass through holes in the absorber, which were present in the early running. Of course, for these events (approximately 5%) the EMI provides no information on the identity of the particle. Figure 7 shows the p_μ and p_h distribution of the hadrons used to determine ρ and λ. The excess of $p_h = 1$ is due to events which had no match at all in the (up to 4) chambers searched. Figures 6 and 7 give some idea of the distribution of hadrons in terms of p_μ and muons in terms of p_h, which in some sense is the figure of merit for the early EMI. For instance, if

CONCLUSION

In summary, we have shown that the optical pulsations of HZ Her are distributed throughout the optical continuum in a way which suggests that they are produced by the same X-ray reprocessing mechanism which is responsible for most of the unpulsed light from the star. We find no evidence for pulsed emission lines and, on the basis of this experiment and the simultaneous spectra and pulsation data of JD 2441823 (discussed earlier), we can rule out the suggestion of DMM that a few prominent emission features are responsible for the pulsations. The reported pulsed emission lines of DMM may have been transient events, but their Doppler velocity and phase relative to the broadband pulsations do not fit well with other observations. We feel that any further investigations into the question of pulsed emission lines should address these latter issues.

emission lines raises another interesting problem. If a strongly

modulated X-ray beam produces the emission lines in the upper atmosphere

of HZ Her, then the recombination times are sufficiently low[2] that the

lines should appear $\sim$ 20% pulsed in contrast to our upper limit of 7%.

This disagreement might be resolved in at least two ways. First, as

noted above, the emission lines may originate near Her X-1 (e.g., in

an accretion disk) instead of HZ Her. In this case, the expected pulsed

fraction would depend upon the geometry of the disk and could be quite

low at this binary phase. Second, the X-rays producing the emission

lines may not be strongly pulsed. Shulman et. al. (1975) have reported

a substantial flux of soft X-rays with a low (5 - 20%) pulsed fraction,

and these soft X-rays should be most important in producing emission

lines. However, these observations introduce problems of their own:

as noted by the authors, this soft X-ray flux should excite emission

lines whose strengths greatly exceed those actually observed.

---

2. According to the recombination coefficients and densities given in DMM, $\tau_{He II} \sim 10^{-2}$ s and $\tau_{N III} \sim 10^{-3}$ s at optical depth unity.

REFERENCES

Alme, M. L., and Wilson, J. R. 1974, Ap. J., 194, 147.

Avni, Y., and Bahcall, J. N. 1974, Ap. J., 191, 221.

Basko, M. M., and Sunyaev, R. A. 1973, Ap. & Space Sci., 23, 117.

Bopp, B. W., Grupsmith, G., McMillan, R. S., Vanden Bout, P.A., and Wootten, H. A. 1973, Ap. J. (Letters), 186, L123.

Canizares, C. R., and McClintock, J. E. 1975, Ap. J., 200, 177.

Crampton, D., and Hutchings, J. B. 1974, Ap. J., 191, 483.

Dahab, R. E. 1974, Ap. J., 187, 351.

Davidsen, A., Henry, J. P., Middleditch, J., and Smith, H. E. 1972, Ap. J. (Letters), 177, L97.

Davidsen, A., Margon, B., and Middleditch, J. 1975, Ap. J., 198, 653 (DMM).

Doxsey, R., Bradt, H. V., Levine, A., Murthy, G. T., Rappaport, S., and Spada, G. 1973, Ap. J. (Letters), 182, L25.

Giacconi, R. 1975, in Astrophysics and Gravitation, Proceedings of the Sixteenth Annual Solvay Conference on Physics, The Solvay Foundation (L'Universite de Bruxelles), p. 27.

Giacconi, R., Gursky, H., Kellogg, E., Levinson, R., Schreier, E., and Tananbaum, H. 1973, Ap. J., 184, 227.

Groth, E. J. 1974, Ap. J., 192, 517.

McClintock, J. E., Canizares, C. R., and Tarter, C. B. 1975, Ap. J., 198, 641.

Middleditch, J., and Nelson, J. 1973, Ap. Letters, 14, 129.

Middleditch, J., and Nelson, J. 1976, Ap. J., in press (Paper I).

Moffett, T. J., Nather, R. E., and Vanden Bout, P. A. 1974, Ap. J. (Letters), 190, L63.

Robinson, L. B., and Wampler, E. J. 1972, Pub. A. S. P., 84, 161.

Shulman, S., Friedman, H., Fritz, G., Henry, R. C., and Yentis, D. J. 1975, Ap. J. (Letters), 199, L101.

Tananbaum, H., Gursky, H., Kellogg, E. M., Levinson, R., Schreier, E., and Giacconi, R. 1972, Ap. J. (Letters), 174, 143.

Table 1

Broadband Pulsations of HZ Her

Start of run	JD 2442686.615
End of run	JD 2442686.743
Initial binary phase	0.181
Final binary phase	0.256
Power/local power*	63.5
Frequency*	
Apparent	0.807895(5) Hz
At solar system barycenter	0.807932(5) Hz
Doppler velocity (relative to HZ Her/Her X-1 center of mass)*	$-21.7(1.8)$ km s^{-1}
Average pulsed fraction[†]	$1.99(14) \times 10^{-3}$

Notes.— Uncertainties ($\pm 1\sigma$) in least significant digit(s) indicated in parentheses. Quantities with an asterisk (*) have been calculated using only the first 2^{20} 10 ms data bins ($\sim$ 95% of data) as a calculational convenience. [†]Pulsed fraction is defined here with respect to the instantaneous light level, not the maximum light from the star as used in Paper I. The pulsed fraction would be 30 - 40% lower according to the latter convention.
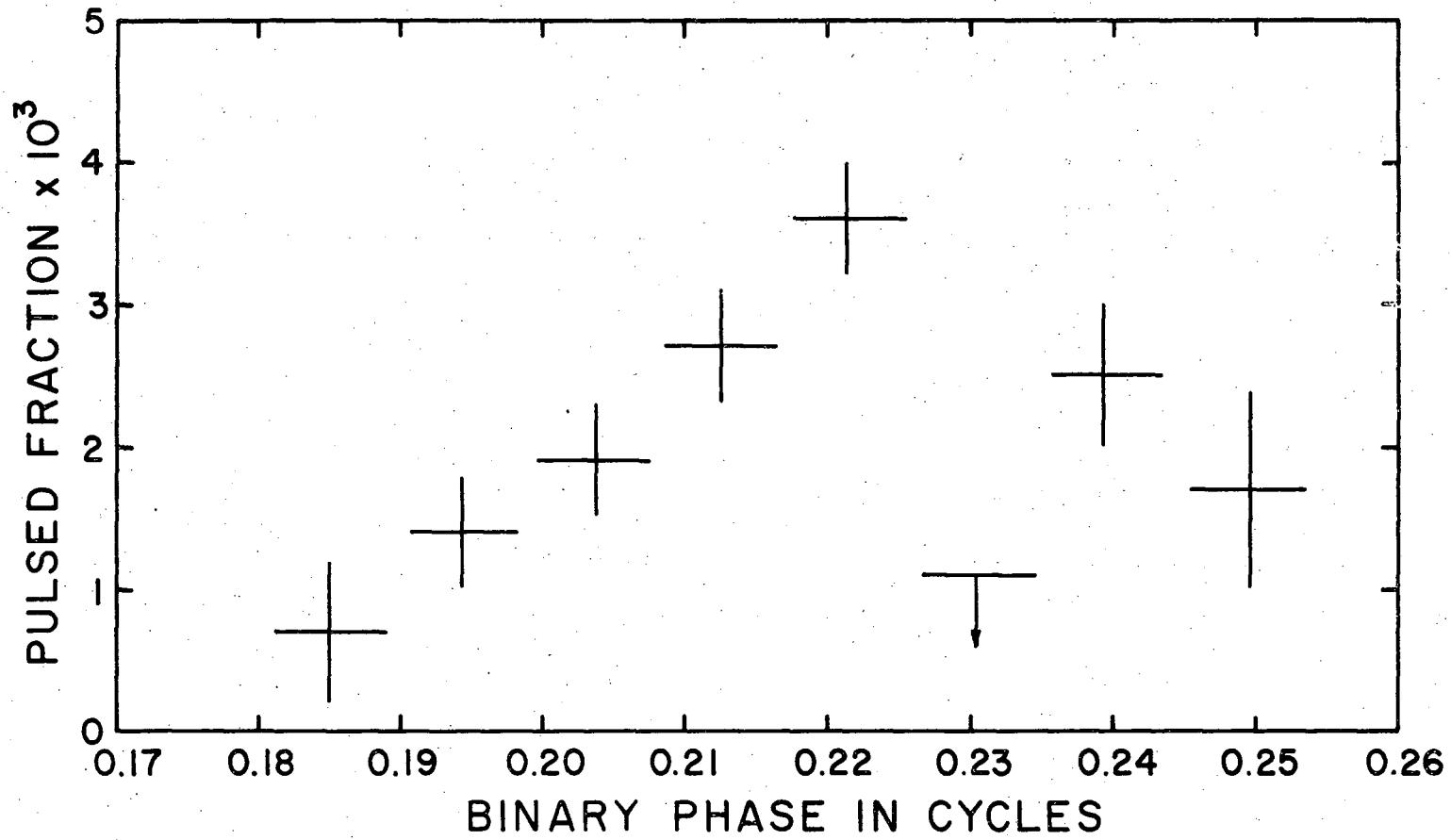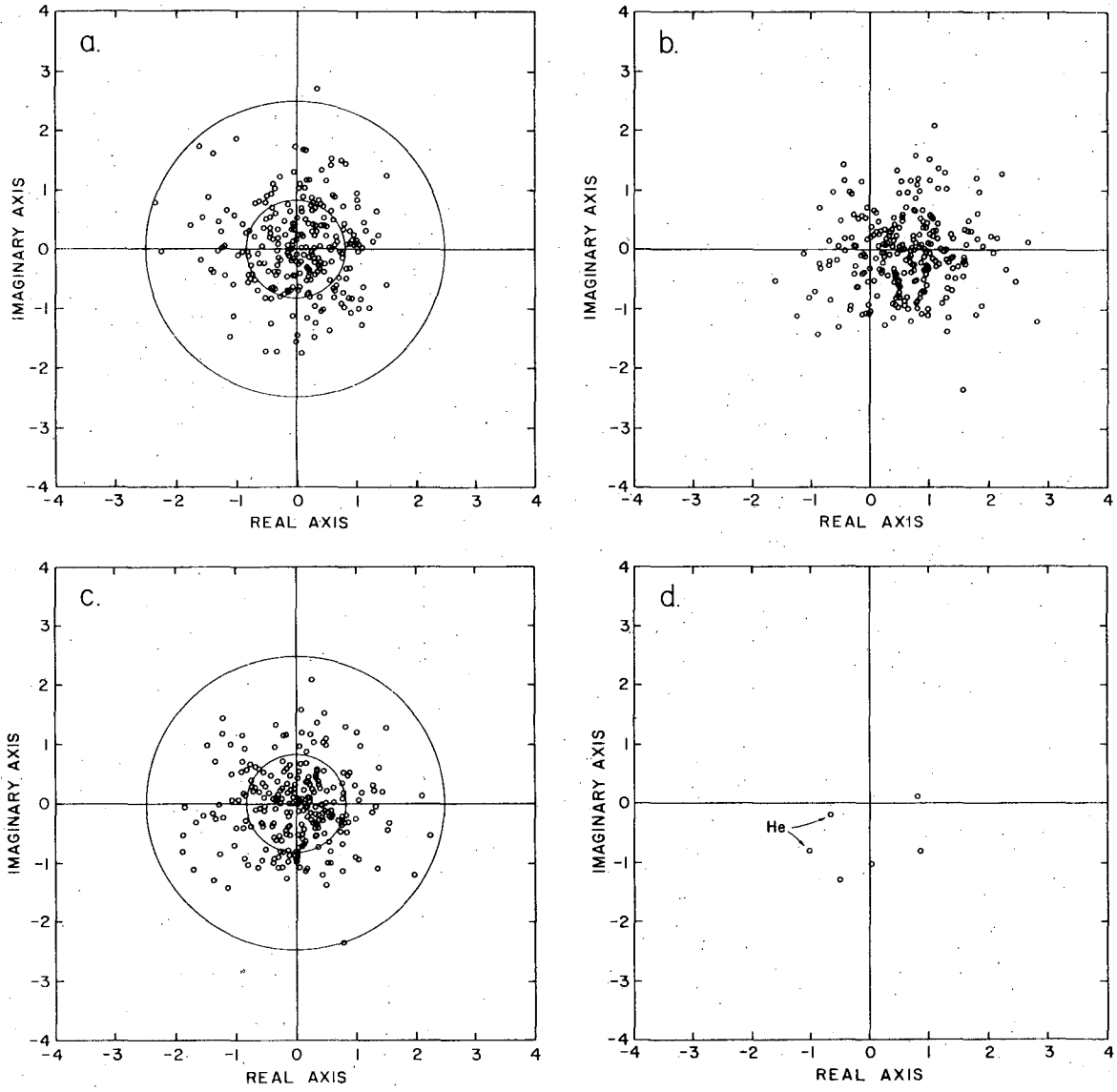
Fig. 2

XBL 765-1627 A

Fig. 3

has been suggested). This can be seen as follows: One can show on general grounds (Avni and Bahcall 1974) that a finite X-ray-to-optical reprocessing time τ leads to a reprocessing efficiency (the ratio of the percentage optical modulation to the percentage X-ray modulation) of

$$\eta = (1 + \omega^2 \tau^2)^{-\frac{1}{2}} \qquad (5)$$

and a corresponding phase shift (of the optical pulses relative to the X-ray pulses) of

$$\Delta\phi = -\tan^{-1}(\omega\tau) \qquad (6)$$

where ω is the angular frequency of the modulation, 5.08 rad s^{-1}. Equations (6) and (7) are true provided the energy conversion process is linear in the sense $\frac{dE}{dt} \propto E$. One expects this to be the case both for pulsed emission lines and, to a good approximation, for simple periodic heating and cooling (pulsed continuum) if the resulting optical modulation is small. Now the low level of continuum pulsations from HZ Her can be understood if $\eta \lesssim 0.04$ allowing for a geometrical attenuation factor of ~ 5 which arises from differing light travel times over the surface (see Paper I). This implies a cooling time of ~ 5 s, and a consequent phase lag of $\sim 88°$ with respect to the incoming modulation, and is consistent with several theoretical values for the cooling time in the range 1 - 10 s (Basko and Sunyaev 1973, Dahab 1974, and Alme and Wilson 1974). On the other hand, the reported modulation

in the emission lines of DMM is $\gtrsim 25\%$, which, again allowing for the geometrical factor of ~ 5, implies $\eta \approx 1$ and hence $\tau \lesssim 0.1$ s, with a resultant phase lag of $\lesssim 30°$. In other words, instead of phase agreement, one would expect pulsed emission lines of the strength reported by DMM to have a phase $60°$ to $90°$ ahead of the phase of any continuum pulsations.

It should also be noted that the observations of DMM appear to disagree with spectroscopic data of other observers. Although the Doppler velocity and acceleration of the broadband signal of DMM establish that the observed pulsations come from the surface of HZ Her, Crampton and Hutchings (1974) present spectroscopic evidence which they feel suggests that both the He II and N III emission lines originate near the compact object (Her X-1) rather than HZ Her. In addition, they detect N III emission very near eclipse, which is difficult to explain if this feature originates from the heated surface of HZ Her. McClintock, Canizares, and Tarter (1975) have noted that one might expect He II emission from near the compact object by analogy with other, more easily observed, optical counterparts of binary X-ray sources. We note that if these features came from near Her X-1 and were strongly pulsed, one would expect significant power at the appropriate Doppler shifted frequency; however in our data, the emission and absorption lines are not significantly pulsed at any nearby frequency. Additional data would be useful in clarifying the origin of the emission from this system.

The low pulsed fraction which we detect in the N III and He II

FIGURE LEGENDS

Fig. 1. Integrated spectrum of HZ Her, binary phase 0.18 - 0.26

Normalization is uncertain below λ 4000. Emission features

N III and He II, Balmer absorption lines, and night sky lines

(O I λ 5577 and several lines of Hg I) are indicated. For

reference, shapes of blackbody curves in an appropriate temper-

ature range (arbitrary normalizations) are also shown.

Fig. 2. Observed pulsed fraction of light from HZ Her as a function

of binary phase. Errors (vertical bars) are statistics dom-

inated; horizontal bars indicate length of integration. The

upper limit indicated in the 6th point corresponds to a 90%

confidence level.

Fig. 3. (a) Normalized Fourier amplitudes (see text) at an arbitrary

frequency for each of the 255 wavelength channels ($\sim$ 10 Å in

width). No signal is present; scatter is due to statistics.

The probability of a point falling within the inner circle is

½ and in about half of such samples one point should fall out-

side the outer circle. (b) Normalized amplitudes at the HZ Her

frequency, pulse phase adjusted to be $0°$. The distribution

resembles that of (a) but shifted to the right, characteristic

of a signal distributed uniformly throughout the spectrum.

(c) Same as (b) but the contribution of a 0.2% pulsed fraction

has been subtracted from each amplitude. Comparison with (a)

shows that essentially all of the signal can be accounted for

in this manner. (d) Same as (b) but showing only those

amplitudes corresponding to emission features discussed in the text: the He II line (which falls in the two indicated channels) and the N III complex (which falls in the remaining four). These amplitudes do not have large components in the direction specified by the broadband pulse phase (positive real axis); corresponding features consequently do not contribute substantially to the observed pulsations.
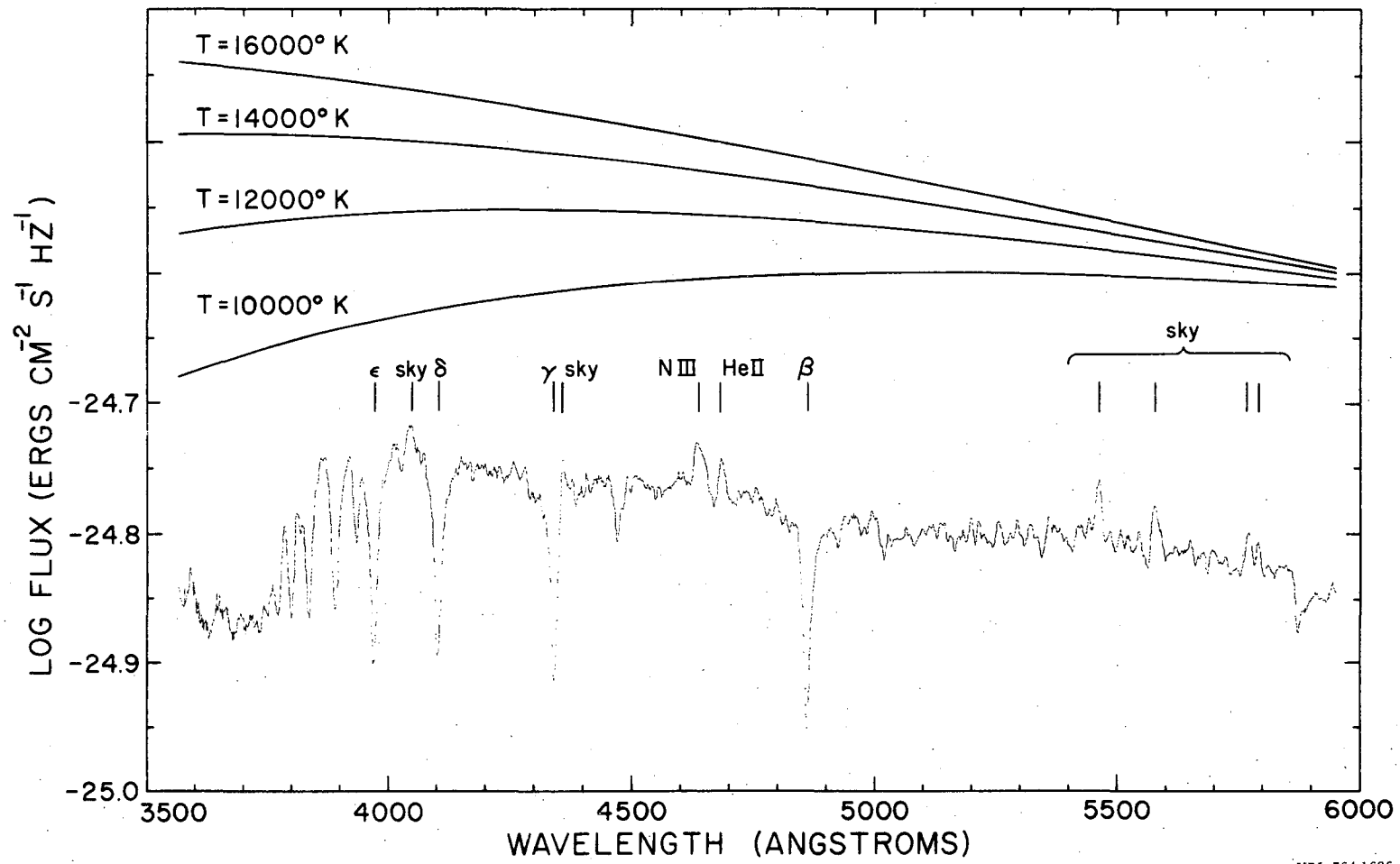
JERRY E. NELSON

GARY A. CHANAN

JOHN MIDDLEDITCH

Lawrence Berkeley Laboratory, University of California,

Berkeley, CA 94720

Fig. 1

XBL 764-1626

Our results are in disagreement with the reported detection of pulsed emission lines and with the resulting hypothesis of DMM. In addition, a search of the literature has established that on at least one occasion (JD 2441823.85 - 2441823.97) when relatively strong pulsations were present (run 46 of Paper I) simultaneous observations (Bopp et. al. 1973) showed no emission lines in the spectrum of HZ Her down to a limit of 0.25 Å equivalent width. This provides independent evidence that the pulsations are not due to a small number of prominent emission features.

DATA ACQUISITION AND ANALYSIS

Spectra of HZ Her were recorded for a 3 hour period on 1 October 1975 beginning at JD 2442686.615, covering the binary phase interval 0.18 - 0.26. This night was selected because the optical pulsations were predicted to be relatively strong on the basis of data in Paper I, and because both the binary and 35-day phases (the latter just prior to X-ray turn-on) closely resembled those during which the reported detections of pulsed emission lines were made by DMM. The observations were made with the Lick Observatory 3 m telescope and image-dissector scanner (IDS) (Robinson and Wampler 1972.) The spectra covered the region 3500 - 6000 Å and were calibrated and normalized with He-Ne-Ar-Hg and quartz lamps and a standard star.

To obtain adequate time resolution, we recorded a 256 point digital spectrum every 10 ms on magnetic tape. Each point was the sum of 8 ordinary scanner channels or ∿ 10 Å in width. (Because the first channel

and cooling of the atmosphere of HZ Her (i.e., the pulsed X-rays from Her X-1 deposit their energy in an optically thick region), or, alternatively, may be due to pulsing emission lines which result from the recombination of X-ray ionized atoms in an optically thin region (Basko and Sunyaev 1973.) (See Crampton and Hutchings (1974) for a description of the (highly variable) emission features from this system.)

The present work concerns the wavelength distribution of the optical pulsations, data which allows one, at least in principle, to distinguish between the various possible pulsation mechanisms. Previous experiments which addressed this question were carried out by Canizares and McClintock (1975), who searched for pulsations in the most prominent emission features, the N III - C III complex (centered near 4640 Å) and He II λ 4686, with negative results[1], and by Moffett, Nather, and Vanden Bout (1974) who obtained similar negative results in the λ 4640 complex alone. Interestingly, one run of Moffett et. al. was simultaneous with run 86 of Paper I in which broadband pulsations were seen. However, Davidsen, Margon, and Middleditch (1975) (hereafter DMM), in more recent observations using a 100 Å interference filter, have reported the detection of such pulsed emission lines (from region I.) A total pulsed equivalent width of ∿ 2 Å and a total pulsed fraction of greater than 25% was reported for the He II and N III lines combined. These features were further reported to be pulsing in phase with the broadband signal, and it was suggested that all of the optical pulsations may in fact be due to a small number of such pulsed emission lines.

---

1. The absence of pulsations reported by Canizares and McClintock may not be significant, since the binary phases during which pulsations are most often present (cf. Paper I) were not covered in their observations.

MEASUREMENT OF THE SPECTRUM OF OPTICAL PULSATIONS

FROM HZ HERCULIS/HERCULES X-1

Jerry E. Nelson, Gary A. Chanan, and John Middleditch

Lawrence Berkeley Laboratory

University of California

Berkeley, California 94720

ABSTRACT

We have measured the wavelength dependence of optical pulsations from this system during binary phase 0.18 - 0.26. These pulsations, which have been shown to originate at the X-ray heated surface of HZ Her, are distributed throughout the optical continuum and have a spectrum similar to that of the unpulsed component. This suggests that the pulsations arise primarily from heating and cooling of the stellar surface, not from emission lines as has been proposed. Emission lines are seen, but are not strongly modulated (<7%) and do not contribute significantly to the observed pulsations.

INTRODUCTION

Weak optical pulsations from the binary system HZ Herculis/ Hercules X-1 were discovered by Davidsen et. al. (1972) and further elucidated by Middleditch and Nelson (1973) and Groth (1974). These pulsations have been studied in detail, and an extensive description of their behavior is given by Middleditch and Nelson (1976) (hereafter Paper I). Those points of paper I which are most important for the present work may be briefly summarized as follows:

(i). The pulsations are essentially sinusoidal, have periods close to the 1.2378175 s period (Giacconi 1975) of the associated X-ray pulsar Her X-1, and have amplitudes corresponding to about 0.1 - 0.2% of the maximum visible light from the system (in contrast to the strong modulation of the X-ray source (Tananbaum et. al. 1972, Doxsey et. al. 1973)).

(ii). The pulsations are intermittent and strongly correlated with the binary phase of the system (binary period = 1.700165 d (Giacconi et. al. 1973)). They are shown to originate both at (or near) the surface of the visible star HZ Her (region I: binary phase $\phi \sim 0.25$, region II: $\phi \sim 0.75$) and near the neutron star companion Her X-1 (region III: $\phi \sim 0.85$). Only those pulsations associated with the surface of HZ Her will be dealt with in the present work.

(iii). Pulsations from the surface of HZ Her are the result of a reprocessing of the incident X-ray energy in the atmosphere of the star, but the broadband observations of Paper I do not provide any insight into the details of this reprocessing mechanism. Two possible mechanisms are discussed in Paper I: The pulsations may result simply from heating

tracks with $p_\mu > 0.1$ are defined to be muons, then 25% of the hadrons

hitting the EMI will be called muons. It should be noted that many

of the hadrons are at very low momentum. If hadrons below 2 GeV/c

are eliminated, then the fraction above $p_\mu = 0.1$ is reduced from 25%

to 16%. This emphasizes how important background is for low momentum

tracks. The sample of hadrons is a reasonably unbiased sample from

neutrino interactions, but the 10 GeV cut in the muon sample eliminates

many of the deeply inelastic neutrino interaction muons.

VII. Conclusions

   The EMI is a device which provides a significant separation

between hadrons and muons. Regenerated muons have been used to

calibrate the proportional chamber positions, spatial resolution,

and efficiency. A simple model incorporating background, inefficiency,

Coulomb scattering, interaction probabilities, and measurement errors

describes well the distribution of hadrons and muons in terms of the

measured variables.

Acknowledgments

   We would like to acknowledge the encouragement and assistance of

the staff of FNAL and particularly the 15-ft bubble chamber crew. We

wish to thank Yong Kang for software support on the online computer

system. We are also grateful to our collaborators on Experiment 45 who

allowed us free use of the data. Finally, we acknowledge the craftmanship

of Todd Hauser of the University of Hawaii, and Norm Andersen, Chuck Covey,

Jim Cullen, Otto Draeger, Leo Foley, Ron Jones, and Herb MacKenzie of LBL.

We are also grateful to D. Yount who participated in the early stages

of the work.

References

1. F. J. Hasert, et al., Phys. Lett. B $\underline{46}$ (1973) 138; A. B. Benvenuti, et al., Phys. Rev. Lett. $\underline{32}$ (1974) 800 and J. von Krogh, et al., Phys. Rev. Lett. $\underline{36}$ (1976) 710.

2. A. Benvenuti, et al., Phys. Rev. Lett. $\underline{34}$ (1975) 419.

3. Fermilab Proposals 9B and 155 (unpublished).

4. F. A. Harris, et al., Nucl. Inst. and Meth. $\underline{103}$ (1972) 345.

5. R. J. Cence and V. J. Stenger, HEPG Report No. UH-551-18-75 (1975), unpublished.

6. S. I. Parker and R. Jones, LBL-797, and S. I. Parker et al. (to be published).

7. E. Binnall, et al., IEEE Trans. on Nucl. Sci. $\underline{NS-20}$ (1973) 367.

8. M. W. Peters, HEPG Report No. UH-511-203-75 (1975), unpublished, and B. Pardoe and M. Leavitt, LBL Group A Physics Programming Memo P-235 (1974), unpublished.

9. B. Pardoe, LBL Group A Physics Programming Memo P-236 (1974), unpublished.

10. L. Eyges, Phys. Rev. Lett. $\underline{74}$ (1948) 1534.

11. The selection of the negatively charged particle with the highest transverse momentum has been discussed by H. Burmeister and D. C. Cundy, CERN Internal Report 75-1 (1975), unpublished.

12. A. Grant, Nucl. Inst. and Meth. $\underline{131}$ (1975) 167.
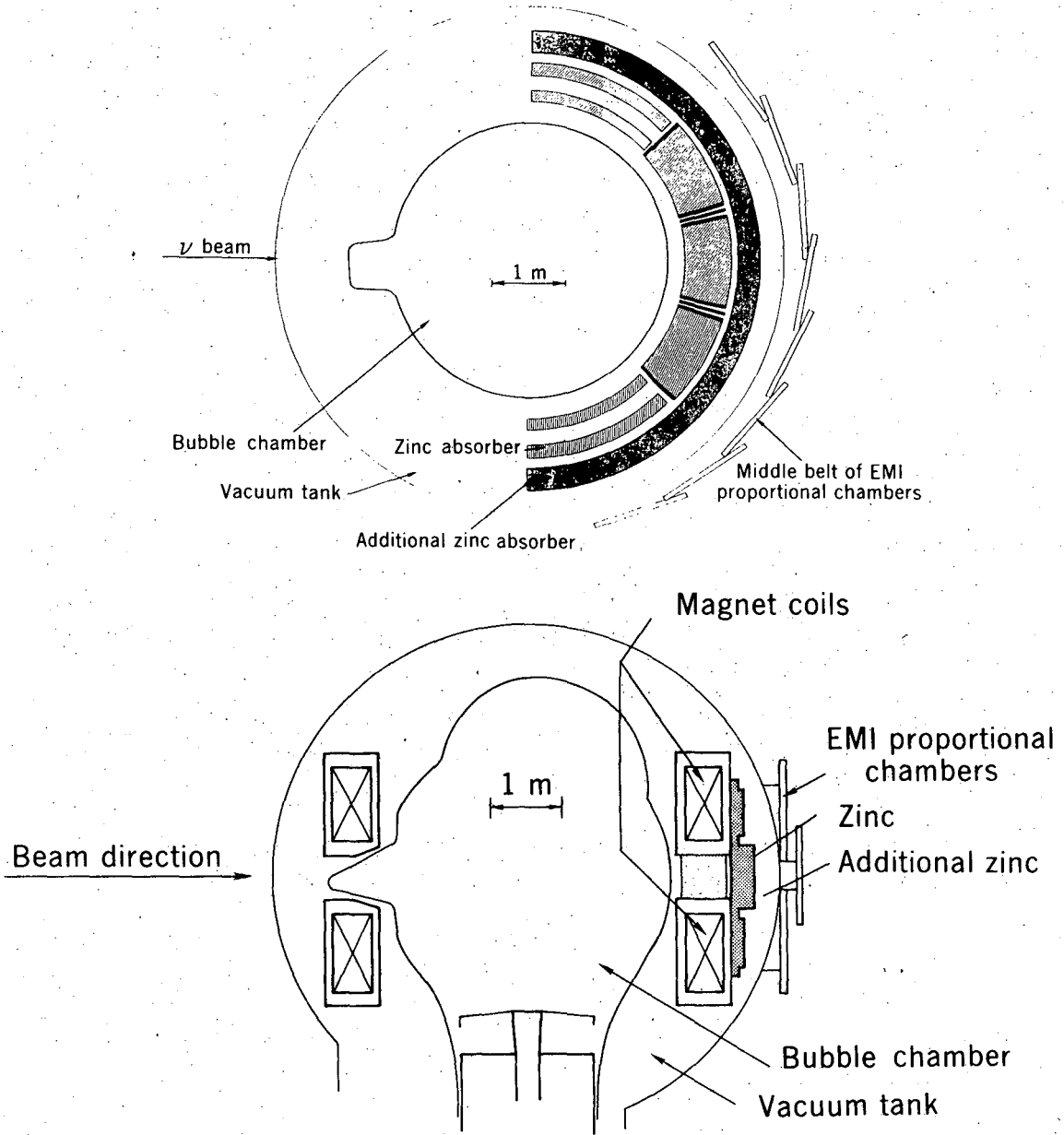
Table 1. Densities and nominal absorption
lengths for various absorber materials.

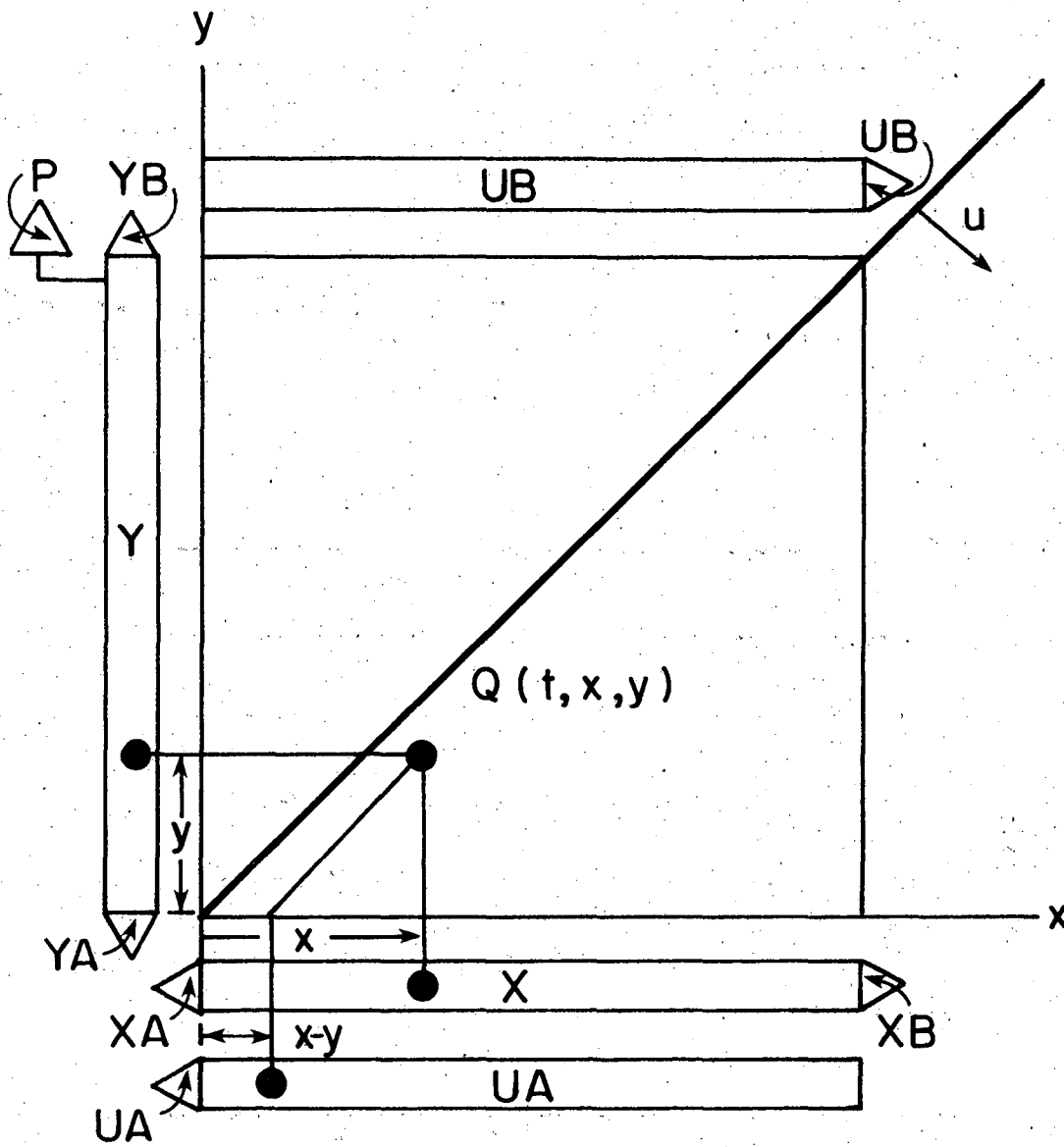| Material	Density (gm/cm^3)	Absorption Length (cm)
Magnetic Coils	6.46	23.1
Stainless Steel	7.75	18.6
Zinc	7.14	21.5
Copper	8.96	16.9

Figure Captions

Fig. 1.   Plan and elevation views of the 15-ft bubble chamber and EMI.

The plan view shows the zinc absorber at the bubble chamber

midplane.   The proportional chambers are mounted directly on

the vacuum tank to maximize the solid angle coverage.   The

additional zinc behind the magnet coils was added after the

data used in the paper was obtained.

Fig. 2.   An avalanche of electrons at Q induces pulses on the delay

lines x, y, and UA at distances x, y, and x - y from the

A ends of the respective delay lines.

Fig. 3.   The calibration of an EMI chamber position by observing the

differences (Δx, Δy) between predicted and observed

coordinates.   The curves shown are a least squares linear fit,

which yields s = 1.0093, x_0 = -0.74, and y_0 = -0.105, where s,

x_0, and y_0 are defined in Eqs. (5).

Fig. 4.   The density of background ρ as a function of area around the

extrapolated track.

Fig. 5.   The absorption length scale factor η as a function of hadron

momentum, where $\eta = \frac{\lambda'}{\lambda}$ and λ' is the experimental absorption

length and λ is the one assumed in Table 1.

Fig. 6.   Distribution in p_μ and p_h for muons.   The sample, which has

less than 1% hadron contaminations consists of single tracks

in the bubble chamber with momenta greater than 10 GeV/c and

which are within 2.5° of the neutrino direction in both dip

and azimuth.

Fig. 7. Distribution in p_μ and p_h for hadrons from selected neutrino interactions. The muon contamination is about 1%.
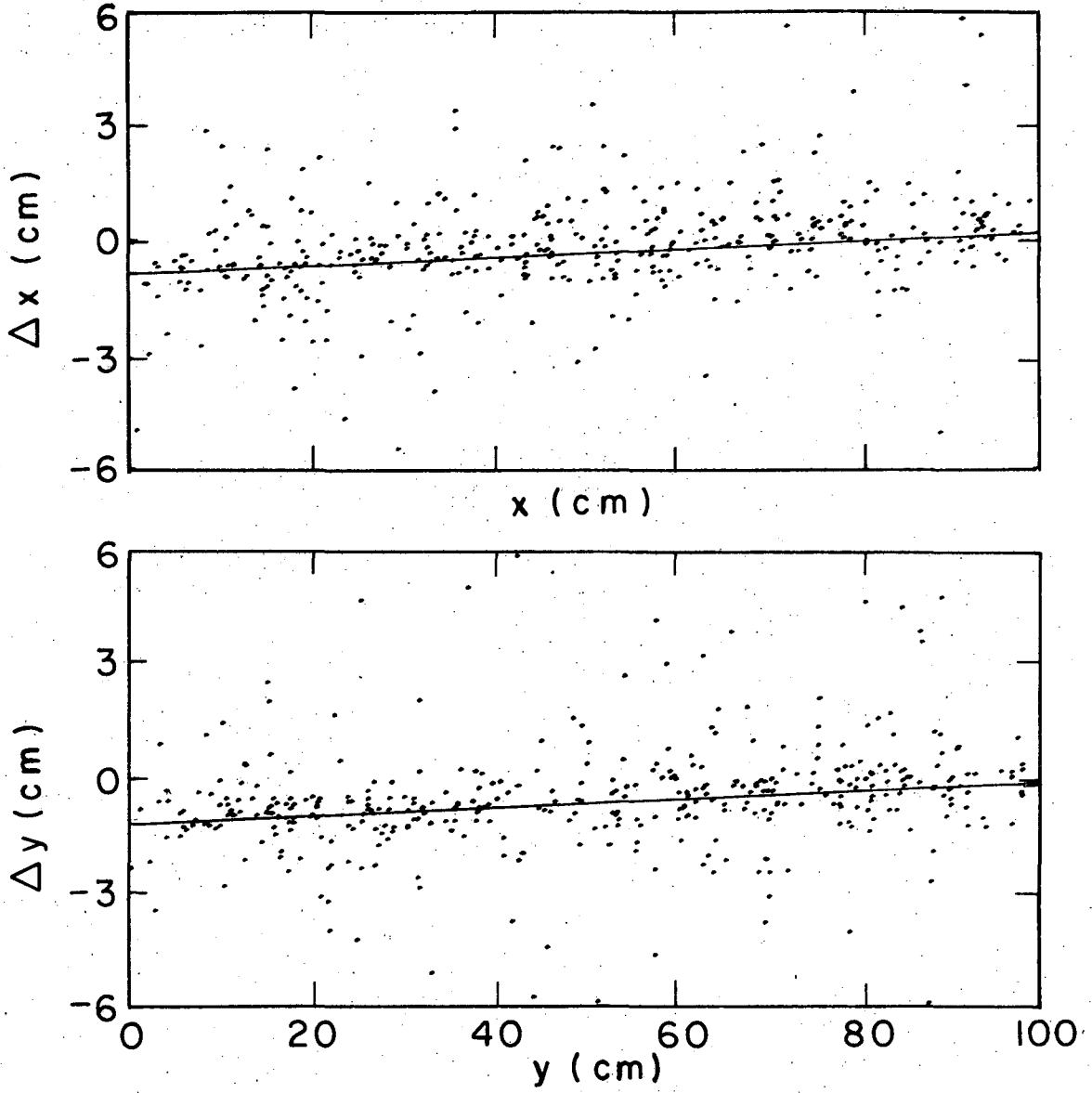
ν beam

1 m

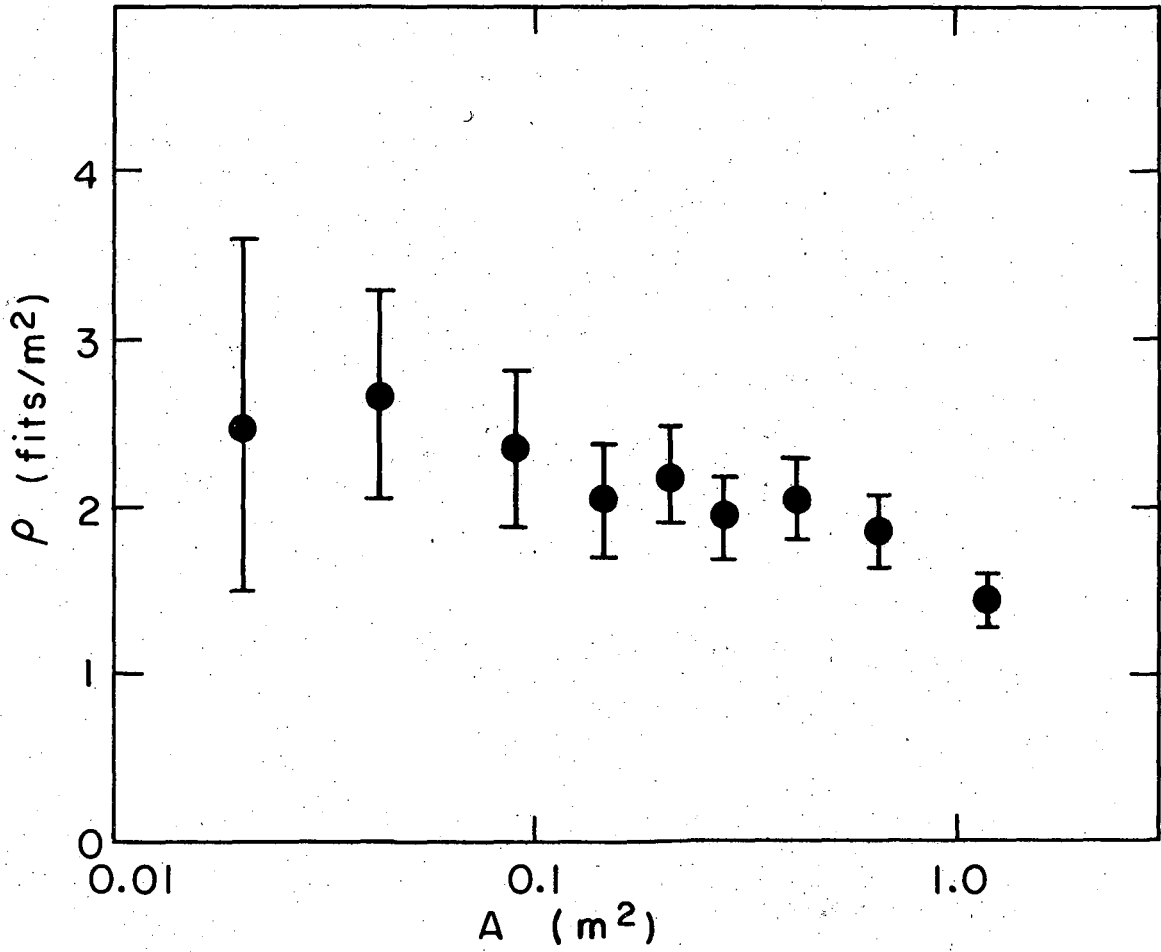Bubble chamber

Zinc absorber

Vacuum tank

Additional zinc absorber

Middle belt of EMI proportional chambers

Magnet coils

1 m

EMI proportional chambers

Zinc

Additional zinc

Beam direction

Bubble chamber

Vacuum tank

XBL 764-2768A
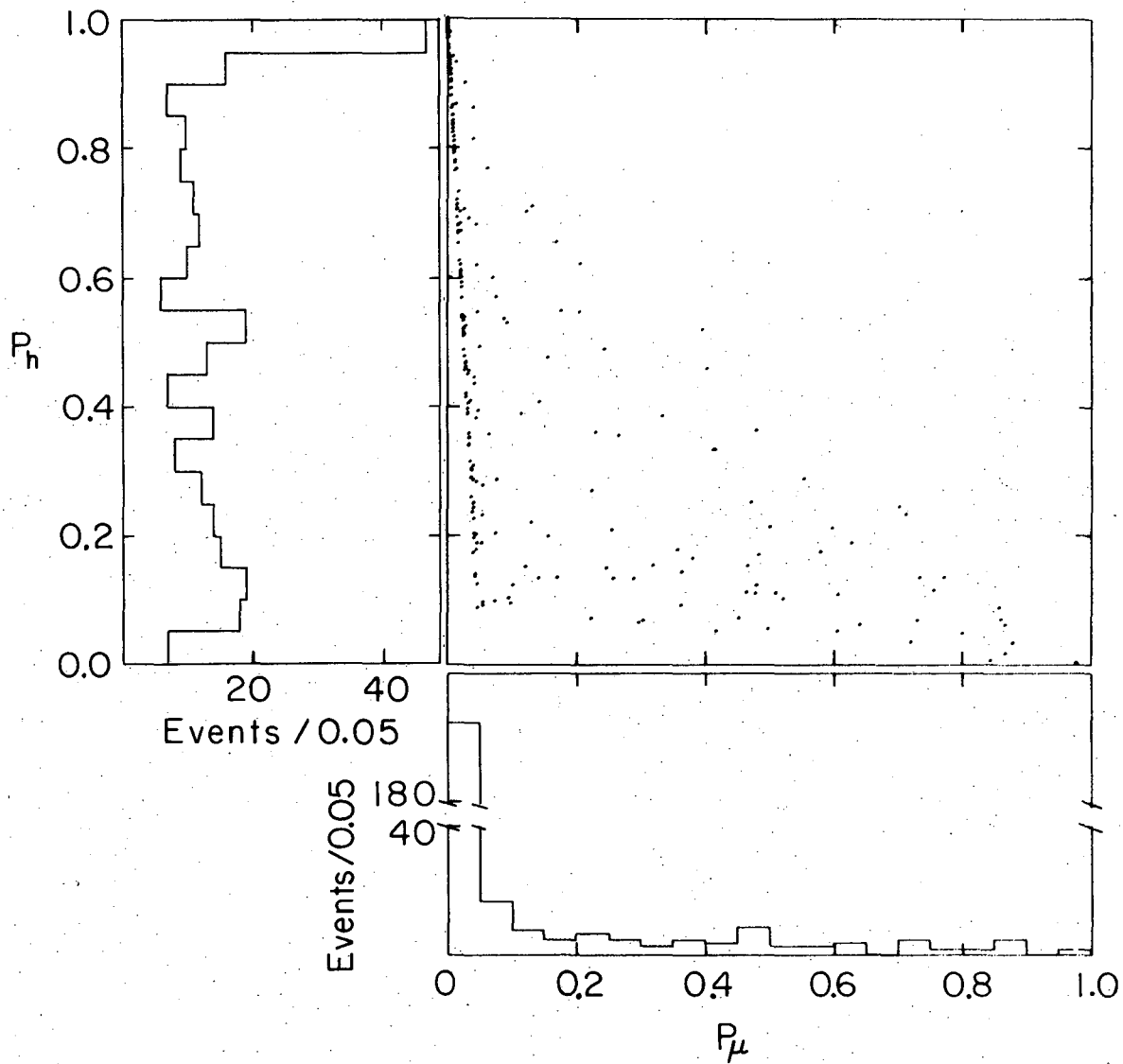
Fig. 1

XBL 764-2659

Fig. 2

Fig. 3

XBL 764-2658

XBL 764-2657

Fig. 4
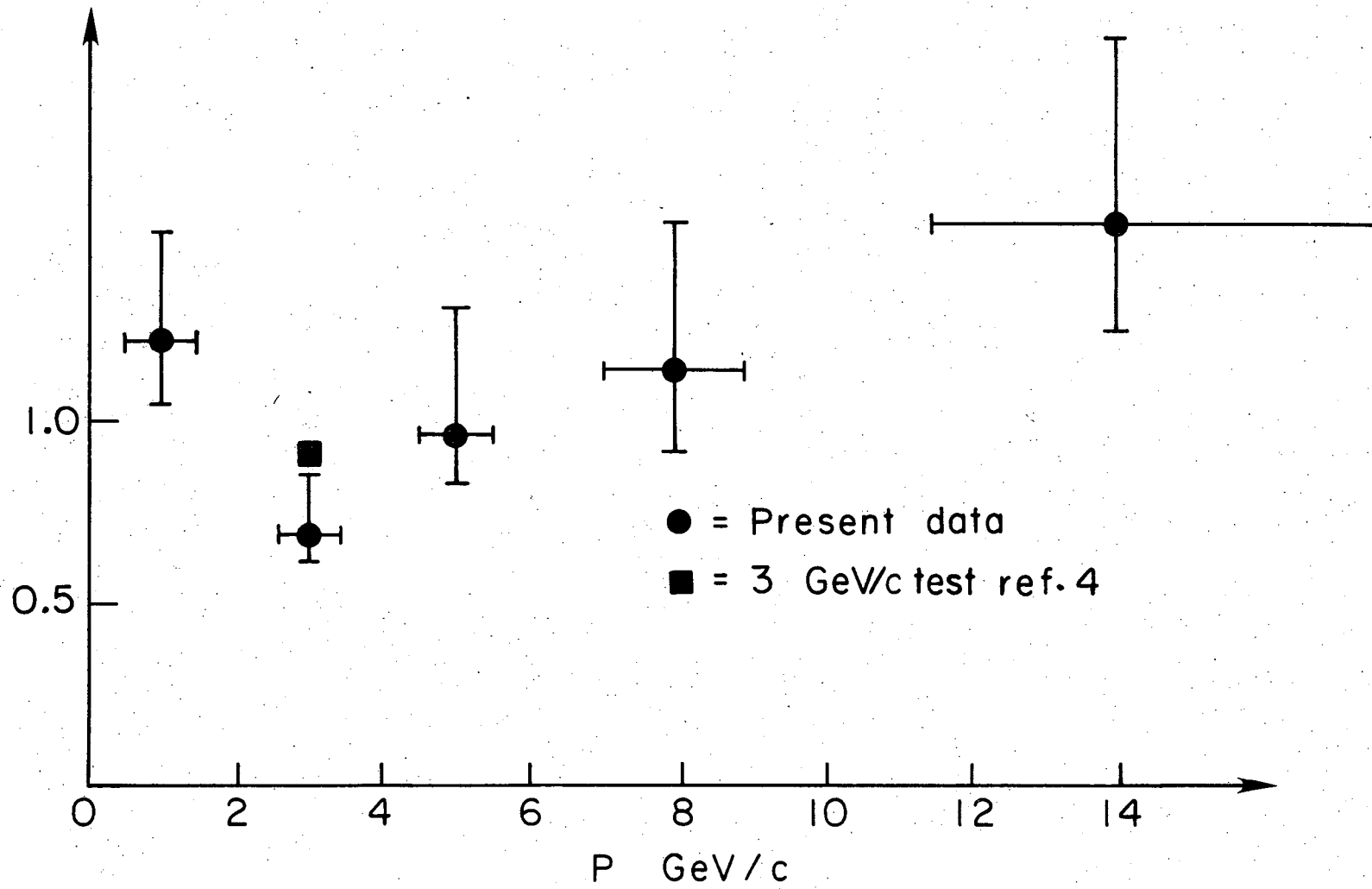
Fig. 5
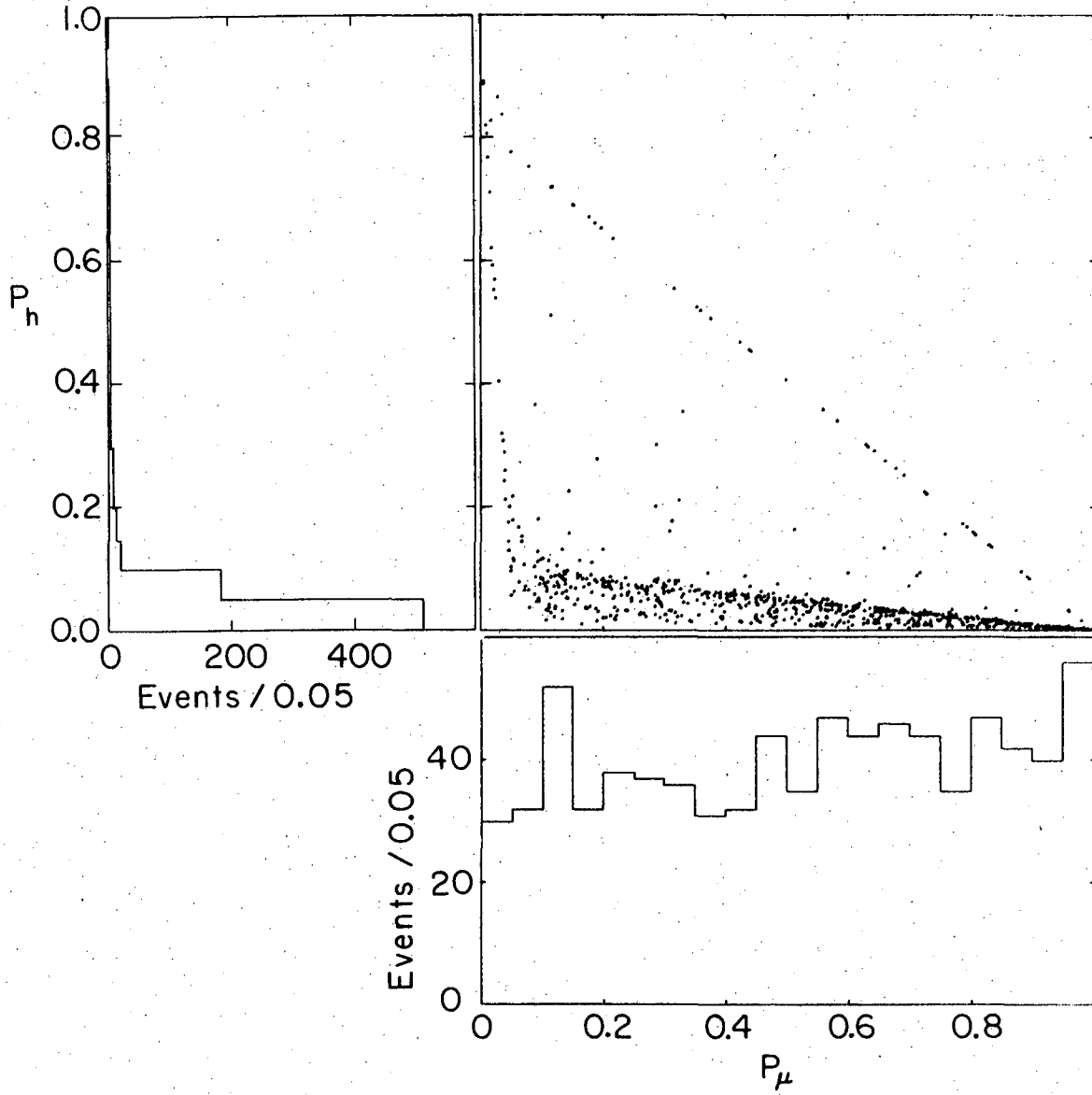
XBL 764-2656

XBL-764-2661

Fig. 6

XBL 764-2660

Fig. 7

TECHNICAL INFORMATION DIVISION
LAWRENCE BERKELEY LABORATORY
UNIVERSITY OF CALIFORNIA
BERKELEY, CALIFORNIA 94720